# Scattering and Interference in Epitaxial Graphene

G. M. Rutter, *et al.*

*Science* **317**, 219 (2007);
DOI: 10.1126/science.1142882

*This copy is for your personal, non-commercial use only.*

**If you wish to distribute this article to others**, you can order high-quality copies for your colleagues, clients, or customers by clicking here.

**Permission to republish or repurpose articles or portions of articles** can be obtained by following the guidelines here.

***The following resources related to this article are available online at www.sciencemag.org (this information is current as of October 19, 2010 ):***

**Updated information and services,** including high-resolution figures, can be found in the online version of this article at:
http://www.sciencemag.org/cgi/content/full/317/5835/219

**Supporting Online Material** can be found at:
http://www.sciencemag.org/cgi/content/full/317/5835/219/DC1

This article **cites 20 articles**, 4 of which can be accessed for free:
http://www.sciencemag.org/cgi/content/full/317/5835/219#otherarticles

This article has been **cited by** 119 article(s) on the ISI Web of Science.

This article has been **cited by** 2 articles hosted by HighWire Press; see:
http://www.sciencemag.org/cgi/content/full/317/5835/219#otherarticles

This article appears in the following **subject collections**:
Physics, Applied
http://www.sciencemag.org/cgi/collection/app_physics

*Science* (print ISSN 0036-8075; online ISSN 1095-9203) is published weekly, except the last week in December, by the American Association for the Advancement of Science, 1200 New York Avenue NW, Washington, DC 20005. Copyright 2007 by the American Association for the Advancement of Science; all rights reserved. The title *Science* is a registered trademark of AAAS.

Our results suggest that effective voluntary suppression of emotional memory only develops with repeated attempts to cognitively control posterior brain areas underlying instantiated memories. In this sense, memory suppression may best be conceived as a dynamic process in which the brain acquires multiple modulatory influences to reduce the likelihood of retrieving unwanted memories.

### References and Notes

1. E. Loftus, *Neuroscience* **4**, 231 (2003).
2. M. C. Anderson *et al.*, *Science* **303**, 232 (2004).
3. M. C. Anderson, C. Green, *Nature* **410**, 366 (2001).
4. J. F. Kihlstrom, *Trends Cognit. Sci.* **6**, 502 (2002).
5. See supporting data on *Science* Online.
6. B. E. Depue, M. T. Banich, T. Curran, *Psychol. Sci.* **17**, 441 (2006).
7. B. A. van der Kolk, J. A. Burbridge, J. Suzuki, *Ann. N.Y. Acad. Sci.* **821**, 99 (1997).
8. B. A. van der Kolk *et al.*, *Am. J. Psychiatry* **153**, 83 (1996).
9. C. Purdon, *Behav. Res. Ther.* **37**, 1029 (1999).
10. P. J. Lang *et al.*, *Psychophysiology* **35**, 199 (1998).
11. E. T. Rolls, *Hum. Neurobiol.* **3**, 209 (1984).
12. S. M. Kosslyn, W. L. Thompson, in *The New Cognitive Neurosciences*, M. S. Gazzaniga, Ed. (MIT Press, Cambridge, MA, ed. 2, 2000), pp. 975–985.
13. C. L. Raye *et al.*, *Cortex* **43**, 135 (2007).
14. A. D. Wagner *et al.*, *Neuroimage* **14**, 1337 (2001).
15. J. L. McGaugh, *Science* **287**, 248 (2000).
16. S. Kastner *et al.*, *J. Neurophysiol.* **91**, 438 (2004).
17. S. Kastner *et al.*, *Science* **282**, 108 (1998).
18. S. Hamann, *Trends Cognit. Sci.* **5**, 394 (2001).
19. E. A. Phelps, *Curr. Opin. Neurobiol.* **14**, 198 (2004).
20. Our activation of FG has been established to be different (more posterior/medial) from the activation of the fusiform face area (FFA) commonly observed in face perception studies (*33*).
21. K. Sakai, R. E. Passingham, *J. Neurosci.* **26**, 1211 (2006).
22. N. Ramnani, A. M. Owen, *Nat. Rev. Neurosci.* **5**, 184 (2004).
23. P. T. Hertel, G. Calcaterra, *Psychonom. Bull. Rev.* **12**, 484 (2005).
24. R. C. O'Reilly, *Science* **314**, 91 (2006).
25. M. Beauregard, J. Lévesque, P. Bourgouin, *J. Neurosci.* **21**, RC165 (2001).
26. L. L. Jacoby, C. M. Kelley, B. D. McElree, in *Dual-Process Theories in Social Psychology*, S. Chaiken, Y. Trope, Eds. (Guilford, New York, 1999), pp. 383–400.
27. H. Garavan, T. J. Ross, E. A. Stein, *Proc. Natl. Acad. Sci. U.S.A.* **96**, 8301 (1999).
28. A. R. Aron, T. W. Robbins, R. A. Poldrack, *Trends Cognit. Sci.* **8**, 170 (2004).
29. K. N. Ochsner *et al.*, *J. Cognit. Neurosci.* **14**, 1215 (2002).
30. N. I. Eisenberger, M. D. Lieberman, K. D. Williams, *Science* **302**, 290 (2003).
31. H. L. Urry *et al.*, *J. Neurosci.* **26**, 4415 (2006).
32. D. Knoch, A. Pascual-Leone, K. Meyer, V. Treyer, E. Fehr, *Science* **314**, 829 (2006); published online 4 October 2006 (10.1126/science.1129156).
33. I. Gautier *et al.*, *Nat. Neurosci.* **3**, 191 (2000).

34. We thank Y. Du, D. Singel, and R. Freedman for assistance in functional imaging, and three anonymous reviewers for their critical insights. Supported by the Graduate School, the Vice-Chancellor for Research, and the Institute of Cognitive Science at the University of Colorado at Boulder (M.T.B.).

**Supporting Online Material**
www.sciencemag.org/cgi/content/full/317/5835/215/DC1
Materials and Methods
Figs. S1 to S5
Tables S1 to S4
References

4 January 2007; accepted 6 June 2007
10.1126/science.1139560

# Scattering and Interference in Epitaxial Graphene

**G. M. Rutter,[1] J. N. Crain,[2] N. P. Guisinger,[2] T. Li,[1] P. N. First,[1]* J. A. Stroscio[2]***

**A single sheet of carbon, graphene, exhibits unexpected electronic properties that arise from quantum state symmetries, which restrict the scattering of its charge carriers. Understanding the role of defects in the transport properties of graphene is central to realizing future electronics based on carbon. Scanning tunneling spectroscopy was used to measure quasiparticle interference patterns in epitaxial graphene grown on SiC(0001). Energy-resolved maps of the local density of states reveal modulations on two different length scales, reflecting both intravalley and intervalley scattering. Although such scattering in graphene can be suppressed because of the symmetries of the Dirac quasiparticles, we show that, when its source is atomic-scale lattice defects, wave functions of different symmetries can mix.**

Built of a honeycomb of $sp^2$-bonded carbon atoms, graphene has a linear, neutrino-like energy spectrum near the Fermi energy, $E_F$. This results from the intersection of electron and hole cones in the graphene band structure at the Dirac energy, $E_D$. The linear energy dispersion and concomitant topological constraints give rise to massless Dirac quasiparticles in graphene, with energy-independent propagation speed $v_F \approx 10^6$ m/s (where $v_F$ is the Fermi velocity). Distinctive symmetries of the graphene wave functions lead to unusual quantum properties, such as an anomalous integer quantum Hall effect (*1*, *2*) and weak antilocalization (*3*, *4*), that have spurred an intense scientific interest in graphene (*5*). Bilayer graphene (*5*–*7*) is equally distinctive: Quasiparticle states are chiral (*6*) with Berry's phase $2\pi$ for the bilayer versus $\pi$ for the monolayer (*6*). High carrier mobilities, chemical inertness, and the two-dimensional (2D) nature of graphene make it a promising candidate for future electronic-device applications (*1*, *2*, *5*, *8*, *9*). In particular, graphene grown epitaxially on SiC substrates and patterned via standard lithographic procedures has been proposed as a platform for carbon-based nanoelectronics and molecular electronics (*8*, *9*).

Epitaxial graphene was grown on the silicon-terminated (0001) face of high-purity semi-insulating 4H-SiC by thermal desorption of silicon at high temperatures (*8*, *10*). This method produces an electron-doped graphene system, with the Fermi level 200 to 400 meV above $E_D$. The data that we present were obtained from a region identified as bilayer graphene (*11*). Scanning tunneling microscopy (STM) measurements were performed in a custom-built ultrahigh-vacuum, low-temperature instrument. We measured the scanning tunneling spectroscopy (STS) differential conductance $dI/dV$ (where $I$ is current and $V$ is voltage) with lock-in detection by applying a small modulation to the tunnel voltage at ≈500 Hz. Differential conductance maps were obtained by recording an STS spectrum at each spatial pixel in the topographic measurement. All measurements reported here were taken at 4.3 K.

STM topographic images (Fig. 1) show the atomic structure and different types of disorder for epitaxial graphene on SiC(0001). At the atomic scale, the graphene is imaged as a triangular lattice (Fig. 1B), characteristic of imaging only one of the two graphene sublattices. Superimposed on this atomic structure is a modulation period of ≈2 nm caused by a reconstruction of the SiC interface beneath the graphene: a SiC "6 × 6" superstructure (*12*). Survey images reveal two categories of defects. Type A defects, such as mounds (red arrow in Fig. 1A), have an unperturbed graphene structure that is continuous, akin to a blanket. These defects are due to irregularities in the interface layer between graphene and the SiC bulk. In contrast, type B defects are atomic defects within the graphene lattice itself (Fig. 1, A, C, and D) and are accompanied by strong distortions in the local lattice images. These distortions are of electronic origin and are accompanied by large increases in the local density of states (LDOS) at the defect site (*13*, *14*). Quasiparticle scattering from type B defects gives rise to spectacular patterns in the topographic images (Fig. 1, C and D) resulting

---

[1] School of Physics, Georgia Institute of Technology, Atlanta, GA 30332, USA. [2] Center for Nanoscale Science and Technology, National Institute of Standards and Technology, Gaithersburg, MD 20899, USA.

*To whom correspondence should be addressed. E-mail: joseph.stroscio@nist.gov (J.A.S.); first@physics.gatech.edu (P.N.F.)

from the symmetry of the graphene Bloch states (*15*–*17*).

Detailed information on scattering from both types of defects is obtained from STS maps of *dI/dV* (Fig. 2), which is determined by the LDOS. By comparing the topographic and spectroscopic images, we find that type B defects in the graphene lattice are the dominant scattering centers. Over much of the energy range studied, these atomic-scale defects have a large central density of states surrounded by a strong reduction in the LDOS that appears to pin the phase of the scattering pattern nearby. For example, the type B defects labeled by blue arrows in Fig. 2 show a bright central spot encircled by a dark region and a bright ring (Fig. 2, B to E). In contrast, the *dI/dV* maps show that type A defects, over which the graphene is continuous (red arrows in Fig. 2), have dramatically less influence on the LDOS.

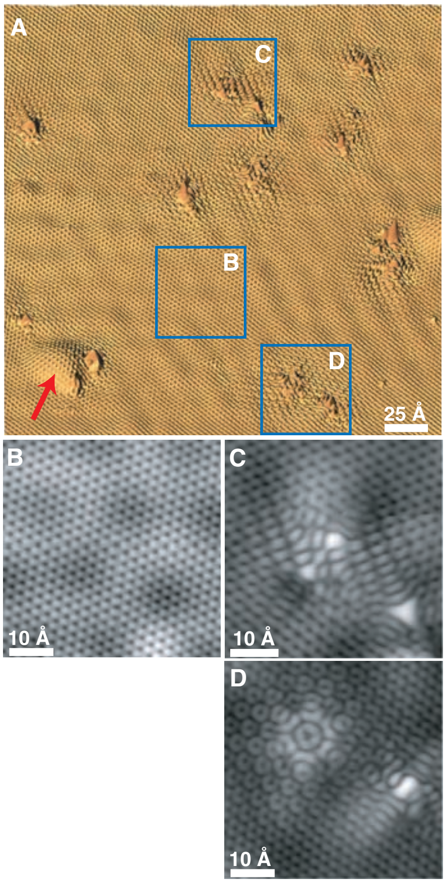

**Fig. 1.** STM topographic images of defects in the bilayer epitaxial graphene sample. (**A**) Large field of view showing a variety of defects. Type A defects (red arrow) are subsurface irregularities blanketed by graphene. The defect indicated by the red arrow has a height of 2 Å. Type B defects are atomic-scale defects in the graphene lattice. Higher-magnification images from the boxed regions in (A) are shown: a defect-free region (**B**) and complex scattering patterns around type B defects [(**C**) and (**D**)]. Tunneling setpoint: $I = 100$ pA, $V = 300$ mV.

Over large length scales, the *dI/dV* maps exhibit long-wavelength fluctuations that change with sample bias voltage (Fig. 2, B to E). As the sample voltage increases from –100 to +100 mV, the dominant wavelength decreases correspondingly from 9 to 5 nm. Fluctuations of much shorter wavelength are also present in these *dI/dV* maps, but they are not apparent over such a large displayed area. Figure 3 shows the short-wavelength modulations in *dI/dV* maps taken with atomic-scale spatial resolution. The interference patterns in these maps display a local $(\sqrt{3} \times \sqrt{3})$R30° structure (Fig. 3, B to E) with respect to the graphene lattice, with a superimposed long-wavelength modulation. Both the long-wavelength standing-wave modulations and the $\sqrt{3} \times \sqrt{3}$ periodicity are due to quasiparticle scattering from type B defects through wave vectors determined by the electronic structure of epitaxial graphene.

The 2D constant-energy contours in reciprocal space (Fig. 4A) are used to understand the scattering vectors that define the interference patterns observed in the STS maps of Figs. 2 and 3 (*18*). For graphene, the constant-energy contours near $E_F$ cut through the electron or hole conical sheets, resulting in small circles of radius κ, centered at the wave vectors $\mathbf{K}_+$ and $\mathbf{K}_-$, that each locate three symmetry-equivalent corners of the 2D Brillouin zone. The scattering wave vectors $\mathbf{q}$ connect different points on the constant-energy contours (Fig. 4A). Two dominant families of scattering vectors, labeled $\mathbf{q}_1$ and $\mathbf{q}_2$, give rise to the patterns observed in the spectroscopic conductance maps. Wave vectors $\mathbf{q}_1$ connect points on a single constant-energy circle (intravalley scattering) and determine the observed long-wavelength patterns. Wave vectors $\mathbf{q}_2$ connect constant-energy circles at adjacent $\mathbf{K}_+$ and $\mathbf{K}_-$ points (intervalley scattering), yielding scattering wave vectors close in length to that of $\mathbf{K}_\pm$. $\mathbf{K}_+$ ($\mathbf{K}_-$) is related to the reciprocal lattice vectors $\mathbf{G}$ by a rotation of 30° (–30°) and a length that is shorter by $1/\sqrt{3}$ in reciprocal space. This relationship gives rise to the $(\sqrt{3} \times \sqrt{3})$R30° real-space superstructures observed in the high-resolution maps (Fig. 3, B to E). The vectors $\mathbf{q}_2$ will differ from the exact $\mathbf{K}_\pm$ wave vector because of the finite size of the constant-energy circles. The combination of different lengths contributing to $\mathbf{q}_2$ leads to the modulation of the $\sqrt{3} \times \sqrt{3}$ scattering patterns in Fig. 3.

To quantify the observed interference patterns and deduce the local band structure, we obtain $\mathbf{q}$-space images of the scattering vectors (Fig. 4B) from Fourier transform power spectra of the spectroscopic *dI/dV* maps (*19*, *20*). In Fig. 4B, $\mathbf{q}_1$ scattering appears as a bright ring centered at $\mathbf{q} = 0$. The ring is a consequence of the enhanced phase space for scattering near the spanning vectors of the constant-energy circle. Circular disks appear centered at the $\mathbf{K}_+$ and $\mathbf{K}_-$ points because of the distribution of $\mathbf{q}_2$ wave vectors. We determined ring radii for the central ring (Fig. 4C) and the $\mathbf{K}_\pm$ point disks using angular averages to maximize the signal-to-noise ratio. Both features change radius as a function of bias voltage because of dispersion in the graphene electronic states, and for these extremal $\mathbf{q}$ values, the scattering geometry determines $|\mathbf{q}| = 2\kappa$ or $|\mathbf{q} \pm \mathbf{K}_\pm| = 2\kappa$. The resulting κ values vary linearly with energy (Fig. 4D), with $v_F = (9.7 \pm 0.6) \times 10^5$ m/s (*18*). The κ = 0 energy intercept gives the Dirac energy, $E_F - E_D = 330 \pm 20$ meV. This local measurement of $E(\kappa)$ agrees well with photoemission studies of bilayer epitaxial graphene (*7*), and the parameters are close to those reported from transport studies on epitaxial graphene grown on SiC(000$\bar{1}$) (*9*). Similar results are found for a single monolayer of graphene (fig. S1) (*18*).

In addition to states localized on defect sites, sharp conductance peaks, ≈5 meV in width, are found several nanometers from the nearest type B defect (Fig. 3). The peaks are clearly associated with the $\mathbf{q}_2$-induced $\sqrt{3} \times \sqrt{3}$ LDOS modulation, as can be seen in the *dI/dV* maps (Fig. 3, B

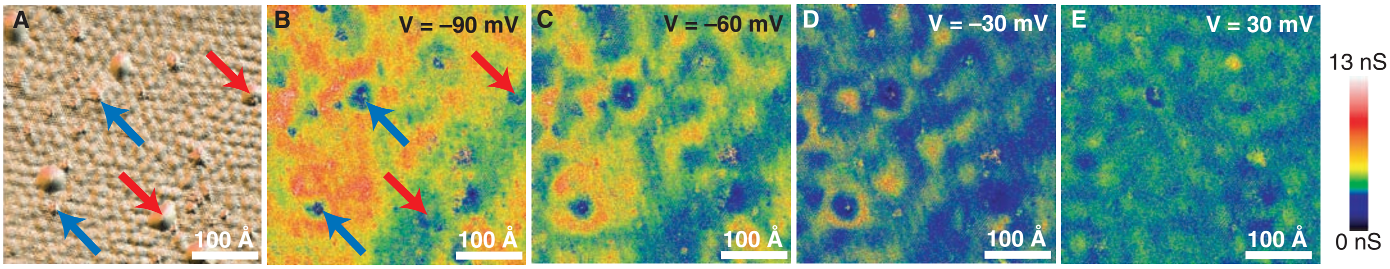

**Fig. 2.** Defect scattering in bilayer epitaxial graphene. (**A**) STM topography and (**B** to **E**) simultaneously acquired spectroscopic *dI/dV* maps. Type A defects (mounds) and type B defects are labeled with red and blue arrows, respectively. Sample biases are: (B) –90 mV, (C) –60 mV, (D) –30 mV, and (E) 30 mV. $I = 500$ pA, $V = 100$ mV, $\Delta V = 1$ $\text{mV}_{\text{rms}}$ where $\Delta V$ is the modulation voltage.

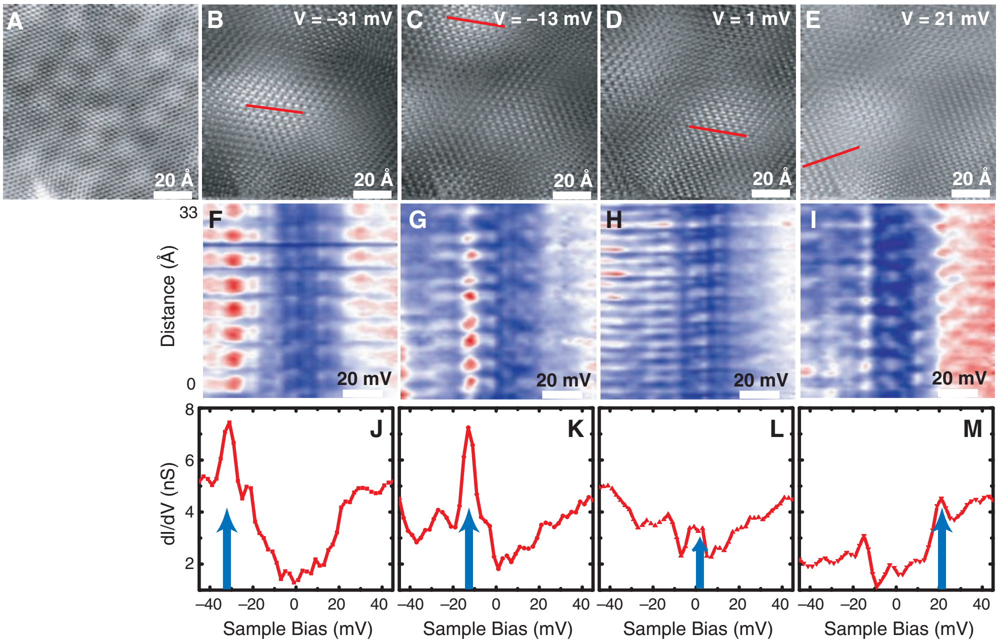

**Fig. 3.** Bilayer graphene topography (**A**) and simultaneous *dI/dV* maps at sample bias voltages of (**B**) –31 mV, (**C**) –13 mV, (**D**) 1.0 mV, and (**E**) 21 mV. The type B scattering centers lie outside the image region [see lower left corner of (A)]. (**F** to **I**) *dI/dV* (color scale) versus sample bias (horizontal axis) and distance (vertical axis) along corresponding red lines in (B) to (E). The blue-white-red color scale spans the conductance values observed in (J) to (M). (**J** to **M**) Line-averaged *dI/dV* spectra obtained from regions marked by red lines in (B) to (E). The spectra are averages of nine curves acquired at positions of the $\sqrt{3} \times \sqrt{3}$ interference maxima in the region of the red lines. Peaks in the *dI/dV* spectra correlate with maxima in the long-wavelength modulation of the $\sqrt{3} \times \sqrt{3}$ interference pattern. Blue arrows indicate the bias (energy) position of the corresponding conductance images in (B) to (E). $I = 500$ pA, $V = 100$ mV, $\Delta V = 0.7$ $\text{mV}_{\text{rms}}$.

to E) and the spectral line profiles (Fig. 3, F to I). Furthermore, the data show that these conductance peaks are spatially localized, with maximum intensity in regions of constructive interference (i.e., over broad maxima modulating the $\sqrt{3} \times \sqrt{3}$ pattern in Fig. 3, B to E). We attribute these conductance peaks to scattering resonances, which localize quasiparticles because of constructive interference in scattering from the random arrangement of defects found within a phase coherence length (*18*).

In support of these conclusions, Fig. 3, F to I, displays sequences of *dI/dV* spectra taken along the red lines shown in Fig. 3, B to E (the red lines are in regions of maximum intensity modulation for the four different energies of the *dI/dV* maps in panels B through E). Each of the figures shows a very prominent $\mathbf{q_2}$ modulation along the vertical (distance) axis at the energy of the corresponding *dI/dV* map (B to E). The lower set of panels (J to M) shows *dI/dV* spectra obtained at positions of the $\sqrt{3} \times \sqrt{3}$ maxima, in the general areas of constructive interference (i.e., near the red lines). Clearly, the energy-dependent standing-wave patterns are associated with conductance peaks of different energies. Across the series of maps and spectra, resonances decrease in intensity as new ones acquire increased spectral strength, each corresponding to a particular spatial location of constructive interference in panels B to E. Resonances are seen at –31 mV (Fig. 3, F and J), at –13 mV (Fig. 3, G and K), straddling the Fermi energy at ±1 mV (Fig. 3, H and L), and at several energies above the Fermi level (Fig. 3, I and M). Many more spectral peaks are observed for different spatial locations in the data set in Fig. 3, with equally narrow line widths.

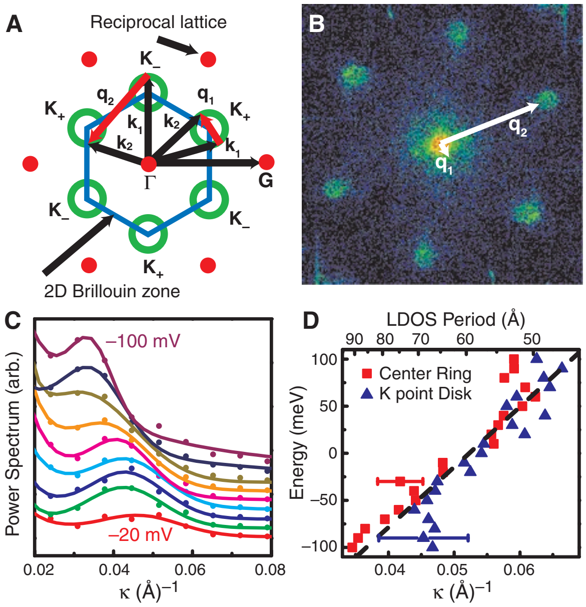

**Fig. 4.** (**A**) Schematic of the 2D Brillouin zone (blue lines), constant-energy contours (green rings) at the $\mathbf{K}_\pm$ points, and the two dominant classes of scattering vectors that create the interference patterns. $\mathbf{k_1}$ and $\mathbf{k_2}$ denote the wave vectors of incident and scattered carriers. Scattering wave vectors $\mathbf{q_1}$ (short red arrow) are seen to connect points on a single constant-energy circle, and wave vectors $\mathbf{q_2}$ (long red arrow) connect points on constant-energy circles between adjacent $\mathbf{K}_+$ and $\mathbf{K}_-$ points. Red circles indicate graphene reciprocal lattice points with origin $\Gamma$. (**B**) **q**-space map of scattering amplitudes, obtained from the Fourier transform power spectrum of the *dI/dV* map in Fig. 2D. $\mathbf{q_1}$ scattering forms the small ring at $\mathbf{q} = 0$, whereas $\mathbf{q_2}$ events create the six circular disks at $\mathbf{K}_\pm$ points. (**C**) Angular averages of the central $\mathbf{q_1}$ ring from the **q**-space maps, at bias voltages from –100 to –20 mV shown in 10-mV increments. arb., arbitrary units. (**D**) Energy dispersion as a function of $\kappa$ for bilayer graphene determined from the **q**-space profiles in (C) and similar data. Values shown are derived from the radii of the central $\mathbf{q_1}$ scattering rings (red squares) and from the angle-averaged radii of the scattering disks at $\mathbf{K}_+$ and $\mathbf{K}_-$ (blue triangles). Dashed line shows a linear fit to the data with $v_F = (9.7 \pm 0.6) \times 10^5$ m/s and an energy intercept of –330 ± 20 meV. Similar results are found for a single monolayer of graphene (fig. S2D) (*18*). The error bars represent the typical combined statistical and systematic uncertainties estimated for each data set.

Of particular interest is the influence of the observed scattering centers on the transport properties of epitaxial graphene. For perfect monolayer graphene, the lattice A-B site symmetry and the $\mathbf{K}_\pm$ valley symmetry give rise to wave functions with distinct values of pseudospin and chirality (*3*, *21*, *22*). Both quantities are tied directly to the group velocity of the quasiparticle wave function, and their near-conservation in the presence of weak potentials is equivalent to a suppression of backscattering.

Our measurements of both $\mathbf{q_1}$ and $\mathbf{q_2}$ scattering processes show very directly that in-plane atomic defects are a dominant source of both intravalley (pseudospin-flip) and intervalley (chirality-reversal) backscattering. This result may explain the observation of weak localization in similar samples (*8*, *18*). The related phenomenon of weak antilocalization was recently confirmed in epitaxial graphene grown by a different method on carbon-terminated SiC$(000\bar{1})$ substrates (*4*), indicating a very low density of in-plane atomic scattering centers in those samples. Thus, the transport properties in epitaxial graphene are critically influenced by the microscopic properties of the sample, determined (at least) by the substrate and growth conditions. For carbon-based electronics, this work highlights the need for further microscopic studies that are correlated closely with macroscopic transport measurements.

### References and Notes

1. K. S. Novoselov *et al.*, *Nature* **438**, 197 (2005).
2. Y. B. Zhang, Y. W. Tan, H. L. Stormer, P. Kim, *Nature* **438**, 201 (2005).
3. E. McCann *et al.*, *Phys. Rev. Lett.* **97**, 146805 (2006).
4. X. Wu *et al.*, *Phys. Rev. Lett.* **98**, 136801 (2007).
5. A. K. Geim, K. S. Novoselov, *Nat. Mater.* **6**, 183 (2007).
6. E. McCann, V. I. Fal'ko, *Phys. Rev. Lett.* **96**, 086805 (2006).
7. T. Ohta *et al.*, *Science* **313**, 951 (2006).
8. C. Berger *et al.*, *J. Phys. Chem. B* **108**, 19912 (2004).
9. C. Berger *et al.*, *Science* **312**, 1191 (2006).
10. E. Rollings *et al.*, *J. Phys. Chem. Solids* **67**, 2172 (2006).
11. The identification of monolayer and bilayer graphene is made from counting the number of atomic steps from the SiC substrate layer combined with STS measurements. Layers are also differentiated by the appearance of Si adatom interface states visible on monolayer graphene (*18*).
12. F. Owman, P. Martensson, *Surf. Sci.* **369**, 126 (1996).
13. V. M. Pereira *et al.*, *Phys. Rev. Lett.* **96**, 036801 (2006).
14. T. O. Wehling *et al.*, *Phys. Rev. B* **75**, 125425 (2007).
15. H. A. Mizes, J. S. Foster, *Science* **244**, 559 (1989).
16. K. F. Kelly, N. J. Halas, *Surf. Sci.* **416**, L1085 (1998).
17. P. Ruffieux *et al.*, *Phys. Rev. Lett.* **84**, 4910 (2000).
18. Additional text and data are available on *Science* Online.
19. L. Petersen, P. Hofmann, E. W. Plummer, F. Besenbacher, *J. Electron Spectrosc. Relat. Phenom.* **109**, 97 (2000).
20. J. E. Hoffman *et al.*, *Science* **297**, 1148 (2002).
21. T. Ando, T. Nakanishi, R. Saito, *J. Phys. Soc. Jpn.* **67**, 2857 (1998).
22. P. L. McEuen *et al.*, *Phys. Rev. Lett.* **83**, 5098 (1999).
23. We thank M. Stiles, E. Jarvis, W. de Heer, X. Wu, C. Berger, and F. Guinea for valuable comments and discussions and S. Blankenship, F. Hess, A. Band, and N. Brown for their technical assistance. This work was supported in part by the Office of Naval Research, by Intel Research, and by NSF grant ECS-0404084.

**Supporting Online Material**

www.sciencemag.org/cgi/content/full/317/5835/219/DC1
Materials and Methods
Figs. S1 and S2
References

22 March 2007; accepted 22 May 2007
10.1126/science.1142882

---

# Efficient Tandem Polymer Solar Cells Fabricated by All-Solution Processing

**Jin Young Kim,[1,2] Kwanghee Lee,[1,2]* Nelson E. Coates,[1] Daniel Moses,[1] Thuc-Quyen Nguyen,[1] Mark Dante,[1] Alan J. Heeger[1]**

Tandem solar cells, in which two solar cells with different absorption characteristics are linked to use a wider range of the solar spectrum, were fabricated with each layer processed from solution with the use of bulk heterojunction materials comprising semiconducting polymers and fullerene derivatives. A transparent titanium oxide ($TiO_x$) layer separates and connects the front cell and the back cell. The $TiO_x$ layer serves as an electron transport and collecting layer for the first cell and as a stable foundation that enables the fabrication of the second cell to complete the tandem cell architecture. We use an inverted structure with the low band-gap polymer-fullerene composite as the charge-separating layer in the front cell and the high band-gap polymer composite as that in the back cell. Power-conversion efficiencies of more than 6% were achieved at illuminations of 200 milliwatts per square centimeter.

Polymer solar cells based on conjugated polymer and fullerene composites offer special opportunities as renewable energy sources because they can be fabricated to extend over large areas by means of low-cost printing and coating technologies that can simultaneously pattern the active materials on lightweight flexible substrates (*1*–*4*). Although encouraging progress has been made with power-conversion efficiencies ($\eta_e$) of 5% having been reported (*5*–*9*), the limited efficiency has hindered the path toward commercialization.

The "tandem cell" architecture, a multilayer structure that is equivalent to two photovoltaic cells in series, offers a number of advantages. Because the two cells are in series, the open-circuit voltage ($V_{oc}$) is increased to the sum of the $V_{oc}$'s of the individual cells. The use of two semiconductors with different band gaps enables absorption over a broad range of photon energies within the solar emission spectrum; the two cells typically use a wide band-gap semiconductor for the first cell and a smaller band-gap semiconductor for the second cell (*10*). Because the electron-hole pairs generated by photons with energies greater than that of the energy gap rapidly relax to the respective band edges, the power-conversion efficiency of the two cells in series is inherently better than that of a single cell made from the smaller band-gap material. Moreover, because of the low mobility of the charge carriers in the polymer-fullerene composites, an increase in the thickness of the active layer increases the internal resistance of the device, which reduces both the $V_{oc}$ and fill factor ($FF$) (*11*). Thus, the tandem cell architecture can have a higher optical density over a wider fraction of the solar emission spectrum than that of a single cell without increasing the internal resistance. The tandem cell architecture can therefore improve the light harvesting in polymer-based photovoltaic cells.

Tandem structures have been investigated for small-molecule heterojunction organic solar cells (*12*–*15*) and for hybrid organic solar cells in which the first cell uses an evaporated small-molecule material and the second cell uses a conjugated polymer; the two cells are separated by a semitransparent metal layer (*16*). Recently, polymer-fullerene composite tandem cells were reported (*17*–*20*). In these devices, a thermally evaporated metal layer is used as a charge-recombination layer and as a protection layer (to prevent interlayer mixing) during the spin-casting of the second cell (*17*–*19*). These polymer-based tandem cells exhibit a high $V_{oc}$, close to the expected sum of the $V_{oc}$'s of the two subcells, but the short-circuit current ($J_{sc}$) is lower than that of either single cell. When the same polymer was used for the front and back cells, the small $J_{sc}$ was attributed to the absorption spectra being identical, so that the back cell absorbs less incident light and thus limits the photocurrent (because the two cells are in series, the current through the multilayer device is determined by that from the back cell). Moreover, because the interfacial metal layer is only semitransparent, the additional absorption also reduces the intensity of the light incident on the back cell. Thus, even when two different polymers are used, the photocurrent is correspondingly reduced.

We report here that we have successfully demonstrated the application of polymer-based bulk heterojunction tandem cells, with each layer processed from solution. A transparent $TiO_x$ layer is used to separate and connect the front cell and the back cell. The $TiO_x$ layer serves as an electron transport and collecting layer for the first cell and as a stable foundation that enables the fabrication of the second cell to complete the tandem cell architecture. In earlier work on tandem cells fabricated with organic semiconductors, the analogous intermediate layer was formed by the evaporative deposition of a semitransparent metal layer in high vacuum. This increases the complexity of device fabrication and causes unwanted loss of light intensity (due to absorption) to the back cell (*14*). For the tandem cells reported here, the $TiO_x$ intermediate layer was deposited from solution (by means of sol-gel chemistry) with no substantial interlayer mixing. The performance of the polymer tandem solar cell is summarized as follows: $J_{sc}$ = 7.8 mA/cm$^2$, $V_{oc}$ = 1.24 V, $FF$ = 0.67, and $\eta_e$ = 6.5%.

---

[1] Center for Polymers and Organic Solids, University of California, Santa Barbara, CA 93106–5090, USA. [2] Department of Materials Science and Engineering, Gwangju Institute of Science and Technology, Gwangju 500-712, Korea.

*To whom correspondence should be addressed. E-mail: klee@gist.ac.kr